Space Sci Rev (2008) 136: 529–547
DOI 10.1007/s11214-007-9251-x

The Electric Antennas for the STEREO/WAVES Experiment

S.D. Bale · R. Ullrich · K. Goetz · N. Alster · B. Cecconi · M. Dekkali · N.R. Lingner · W. Macher · R.E. Manning · J. McCauley · S.J. Monson · T.H. Oswald · M. Pulupa

Received: 11 January 2007 / Accepted: 19 July 2007 / Published online: 9 November 2007

Abstract The STEREO/WAVES experiment is designed to measure the electric component of radio emission from interplanetary radio bursts and in situ plasma waves and fluctuations in the solar wind. Interplanetary radio bursts are generated from electron beams at interplanetary shocks and solar flares and are observed from near the Sun to 1 AU, corresponding to frequencies of approximately 16 MHz to 10 kHz. In situ plasma waves occur in a range of wavelengths larger than the Debye length in the solar wind plasma $\lambda_D \approx 10$ m and appear Doppler-shifted into the frequency regime down to a fraction of a Hertz. These phenomena are measured by STEREO/WAVES with a set of three orthogonal electric monopole antennas. This paper describes the electrical and mechanical design of the antenna system and discusses efforts to model the antenna pattern and response and methods for in-flight calibration.

Keywords Sun: magnetic field · Sun: flares · Sun: coronal mass ejections

1 Introduction

The STEREO mission has as its primary science goal the study of the generation, evolution, and propagation of Coronal Mass Ejections (CMEs). CMEs that propagate into the

---

S.D. Bale · N. Alster · N.R. Lingner · M. Pulupa
Physics Department, University of California, Berkeley, USA

S.D. Bale (✉) · R. Ullrich · J. McCauley · M. Pulupa
Space Sciences Laboratory, University of California, Berkeley, USA
e-mail: bale@ssl.berkeley.edu

K. Goetz · S.J. Monson
School of Physics and Astronomy, University of Minnesota, Minneapolis, USA

B. Cecconi · M. Dekkali · R.E. Manning
LESIA, Observatoire de Paris, Meudon, France

W. Macher · T.H. Oswald
Space Research Institute, Austrian Academy of Sciences, Graz, Austria

heliosphere are called Interplanetary Coronal Mass Ejections (ICMEs) and are known to drive strong interplanetary (IP) shocks as they propagate through the heliosphere and often contain magnetic flux ropes (or "magnetic clouds") carrying plasma thought to be remnants of solar filaments and loops.

As ICME-driven IP shocks propagate, they accelerate electrons by a fast-Fermi process (Wu 1984; Leroy and Mangeney 1984); the efficiency of fast-Fermi acceleration is thought to be a strong function of shock tangent angle, being most efficient at nearly perpendicular shocks (e.g. Krauss-Varban and Burgess 1991). The electrons accelerated at the shock front stream into the solar wind and form beam-like features, due to advection (Fitzenreiter et al. 1984; Bale et al. 1999). These beams are unstable to the growth of Langmuir waves and Langmuir waves propagating in the inhomogeneous solar wind may mode-convert by linear (Kellogg 1986; Bale et al. 1998) and/or nonlinear (Cairns and Melrose 1985; Goldman 1984) processes into freely propagating o-mode radiation at the electron plasma frequency $f_{pe}(r) = \sqrt{4\pi n(r) e^2/m_e}$ and its harmonic $2f_{pe}$, where $n(r)$ is the heliospheric plasma density at a distance r from the Sun.

These radio emissions, from CME-driven IP shocks, are known as "IP type II bursts" and are observed to drift in time from high to low frequencies. Since the emission frequencies are related to the local plasma density, IP type II bursts can be used to track CMEs from near to the Sun to 1 AU. For typical heliospheric density profiles, this corresponds to frequencies of 20 MHz (near the Sun) to 20 kHz (near 1 AU). IP type II bursts exhibit fine structure that may be related to shock structure (Bale et al. 1999), an important consideration for theories of energetic particle acceleration at shocks. The primary measurement goal of the STEREO/WAVES (S/WAVES) experiment is to resolve these IP type II bursts in frequency and time, to measure their direction of arrival (e.g. Fainberg et al. 1972), and use these measurements to infer CME speed and acceleration, shock structure, and heliospheric density. S/WAVES will also measure the fast-drifting radio emission from solar flare electrons, called "type III" radio bursts. Type II and III radio emission are observed at 1 AU to have intensities from approximately 10^{12} Jy (10^{-14} W/m^2 Hz) for very large events and down to the level of the galactic synchrotron spectrum at a few MHz (approximately 10^6 Jy or 10^{-20} W/m^2 Hz) (Novaco and Brown 1978), which defines the instrument noise level requirement.

Another science goal for STEREO/WAVES is the measurement in situ of the plasma waves involved in the plasma radiation process and collisionless shock physics. Langmuir waves are driven unstable by shock-accelerated electron beams and mode-convert to the observed radio emission. The mechanism of mode-conversion from Langmuir to radio waves is still poorly understood and polarization measurements from S/WAVES are essential. Langmuir waves in IP radio bursts and the terrestrial foreshock are observed to have amplitudes from above the thermal noise level to approximately 100 mV/m (e.g. Bale et al. 1997) at the local plasma frequency f_{pe} (10–40 kHz at 1 AU). Electric field noise at collisionless shocks is observed to have similar amplitudes and is primarily Doppler-shifted $f \approx v_{sw}/\lambda_D$, where λ_D is the local Debye length; this corresponds to measured frequencies up to a few kHz at 1 AU.

Some secondary sciences goals are the measurements of low-frequency electric field and density fluctuations (Bale et al. 2005; Kellogg et al. 2006) probably associated with the Alfvénic turbulent cascade and the measurement of the plasma thermal noise spectrum in CME filament material (Meyer-Vernet and Perche 1989; Larson et al. 2000). Although these measurements are scientifically very compelling (indeed perhaps more fundamental than the primary science!), they do not drive S/WAVES instrument requirements (next section). The overall STEREO/WAVES experiment is described in a companion paper (Bougeret et al. 2007).

Table 1 Antenna science requirements

Science objective	Antenna requirement
Radio direction finding	$L < 9$ m
Radio sensitivity	$C_B < 150$ pF and maximum L

2 Antenna Science Requirements

The primary S/WAVES science requires the measurement of the electric field component of radio emission from 16 MHz down to approximately 20 kHz, corresponding to free-space wavelengths of 18.75 m to >15 km. The need to do direction-of-arrival analysis requires an electrically short antenna ($2L \ll \lambda/2$) to minimize sidelobes and phase perturbations near the antenna quarter-wave resonance. The desire to observe the galactic synchrotron spectrum (as the instrument background), however, argues for more sensitivity and therefore longer antennas. The in situ plasma wave measurement goals also benefit from longer antenna elements. These requirements are summarized in Table 1.

At radio frequencies, the voltage gain of the antenna system goes as $G \sim C_A/(C_A + C_{\text{stray}})$, where C_A is the antenna capacitance and C_{stray} is the stray capacitance; C_{stray} includes the "base" capacitance C_B of the antenna with respect to the enclosure as well as cable and preamp input capacitance and is discussed more in Sect. 5. Therefore to maximize system sensitivity, the base capacitance must be minimized. Previous experience from the Wind, Ulysses, ISEE, and Cassini radio instruments suggested that C_B must be less than 150 pF (requirement) with a desired goal of $C_B < 100$ pF. A simple expression for the reactance of a monopole antenna (of length L, radius a, and wavenumber k) above an infinite ground plane (Balanis 1997) gives the antenna free-space capacitance

$$C_A \approx \frac{2\pi\epsilon_0}{(\log(L/a) - 1)} \frac{\tan(kL)}{k} \tag{1}$$

which takes a value of approximately 63 pF for a single $L = 6$ m monopole (with a 2.3 cm average diameter) at long wavelengths $kL \ll 1$. A preliminary measurement of the antenna base capacitance, done in the lab on an engineering model, gave a value of about 50 pF. Further measurements of base capacitance are described in Sect. 5. The above values imply a gain of $G \sim 1/2$ at radio frequencies, which is considered to be quite good.

The secondary science goals of measuring low frequency (to DC) electric fields would be better carried out with a "double-probe" antenna system similar to that on the Polar, Cluster, and FAST satellites (e.g. Harvey et al. 1995). A double-probe uses a current-biased probe extended on a boom (or wire) away from the spacecraft (see Pedersen et al. 1998).

3 Sensor Electrical Design

The S/WAVES antennas measure both the electric fields of freely propagating radio emission at frequencies above f_{pe} and in situ plasma waves and DC fields. In addition, the antenna floating voltage is sensitive to the ambient electron density, as discussed in the following.

Electric fields in the plasma couple to the antenna both resistively and capacitively (Fig. 1 illustrates this). In sunlight, the antennas emit photoelectrons with a characteristic (e-folding) energy of a few volts (e.g. Grard 1973). The antennas therefore charge positively with respect to the plasma and draw a return current from the thermal electron and the emitted photoelectron population. An electron sheath forms around the antenna with a thickness

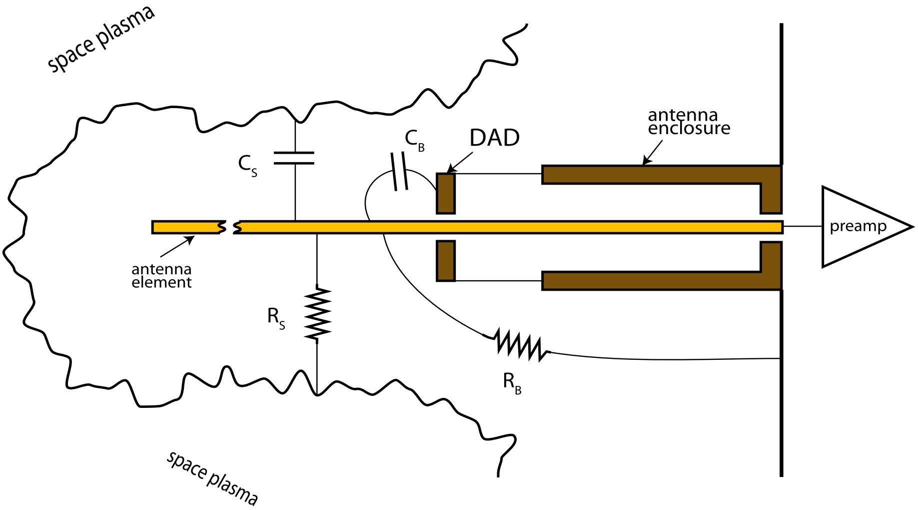

Fig. 1 A cartoon of the electrical design of an S/WAVES antenna. The antenna element is coupled both resistively and capacitively to the plasma, as well as being coupled to the antenna enclosure and spacecraft, as discussed in the text. At radio frequencies ($f \gg f_{pe}$), the antenna capacitance is effectively that of a monopole in vacuum and the coupling is purely capacitive

given approximately by the Debye length of the photoelectrons λ_p (e.g. Gurnett 1998 and references therein).

At DC and very low frequencies (typically less than a few hundred Hz), the antenna–plasma coupling is primarily resistive with the "sheath" resistance being given by the slope of the current–voltage curve (which of course depends on the thermal electron flux in the plasma). For an unbiased antenna in sunlight, this is approximately $R_s \approx V_p/I_e$, where V_p is the photoelectron energy (typically a few volts) and $I_e = A\, n_e e\, v_{\mathrm{the}}$ is the thermal electron current on the antenna (of area A). In the solar wind at 1 AU, we would expect values like $R_s \approx 0.75$ MΩ.

Photoelectrons that leave one surface and are collected on another can be a source of current that flows between the antenna and the ground surfaces (antenna enclosure, spacecraft, solar panels, etc.). This is a short circuit to the measurement and is represented by a "base" resistance R_B. From Fig. 2, it can be seen that the antenna gain at low frequencies is approximately $G \sim R_B/(R_B + R_S)$. Since the sheath resistance R_S can be a strong function of the plasma thermal current (which varies), it is desired to make the base resistance R_B as large as possible. Ideally, this is accomplished by having very long booms (wire or rigid) to hold the sensor far from any ground surfaces. Insulating coatings and/or voltage-biased surfaces may also be used to erect a barrier between the probes and the spacecraft ground. For S/WAVES, no such accommodations have been made, since DC/LF measurements are not a primary science goal. Kellogg and Bale (2001) measured the base resistance on the Wind spacecraft, which uses long, thin wire antennas in the spin plane and short rigid antennas along the spin axis. They found a base resistance (for the wire antennas) that varies weakly with electron flux ($R_B \approx A + B/\mathit{flux}$, where A and B are constants) and takes values from 50 MΩ to 300 MΩ, depending on whether the antenna base is shadowed or in sunlight. Scaling those results to the S/WAVES antenna diameters (with shaded bases) gives a base resistance between 1–10 MΩ.

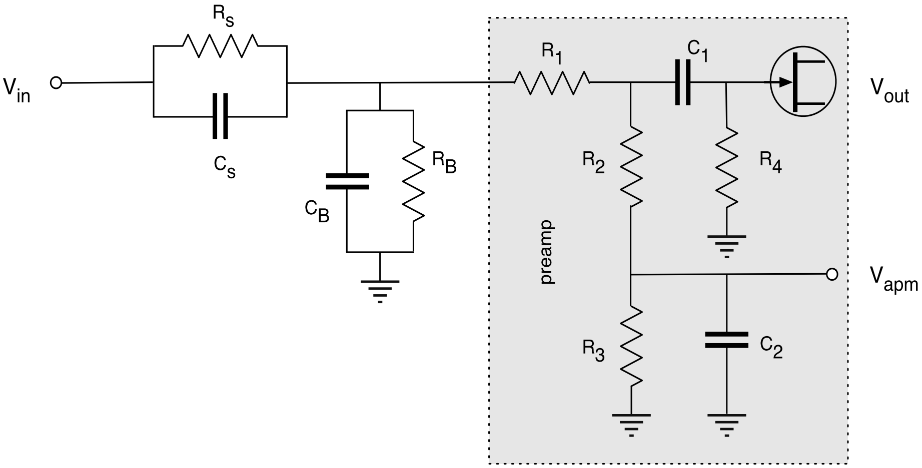

Fig. 2 Schematic of the electrical design of an S/WAVES antenna and preamp. The antenna impedance and base impedance have both resistive and capacitive components (see Fig. 1). Circuit elements in the *gray box* are real components within the preamplifier and have the values given in Table 2. Waveform and spectral measurements are high-pass filtered into a high-impedance FET (V_{out}). The antenna floating voltage is also produced at V_{apm}

Table 2 Values for circuit elements in Fig. 2

	Component	Value
Sheath resistance	R_s	~ 0.75 MΩ
Antenna capacitance	C_s	~ 40 pF
Base resistance	R_b	~1–10 MΩ
Base capacitance	C_B	~ 60 pF
	C_1	100 pF
	C_2	100 pF
	R_1	100 Ω
	R_2	33 MΩ
	R_3	33 MΩ
	R_4	150 MΩ

At high frequencies ($f \gg f_{pe}$), the electric field of a radio wave is only coupled to the plasma very weakly. In this case, we can ignore the plasma and consider the antenna to be in a vacuum. As discussed in Sect. 2, the antenna gain is then given by $G \sim C_A/(C_A + C_B)$ and the design goal is to minimize the stray or "base" capacitance C_B between the antenna elements and any conducting structure (discussed in Sect. 5). For S/WAVES this was achieved by paying special attention to overall design and materials; for example, the roller surfaces which are in contact with the antenna element were anodized and isolated on insulating axes.

The basic design of the S/WAVES antenna system is a set of three orthogonal monopoles. Ideally, one would use three orthogonal dipole antennas, however mass and accommodation constraints did not permit this. While a monopole extended normal to an infinite groundplane will behave as a dipole, the spacecraft is *not* an infinite groundplane and the final antenna pattern is different from that of a dipole. This effect is discussed is Sect. 5.

4 Antenna Mechanical Design

Each antenna assembly consists of a 6 m long Beryllium–Copper (BeCu) "stacer" element installed in a magnesium and aluminum housing that provides launch storage, deployment means, and support at the proper orientation. Figure 3 shows a CAD drawing of an antenna unit with the external covers removed. The basic components of a unit are the stacer antenna element, a flyweight brake mechanism, a deployment assist device (DAD), and a release mechanism (SMAR) to deploy the sensor. These components are described in the following. Figure 4 is a photograph of a deployed antenna unit.

Each spacecraft has three antenna assemblies mounted to a single interface plate which is integrated to the anti-sun side ($-$X deck) of the spacecraft. When deployed, the three antennas form a mutually orthogonal pattern, equi-angular from the spacecraft deck. As shown in Fig. 5, the antenna elements deploy to form three edges of a cube whose corner touches the spacecraft. Projected onto the $-$X deck of the spacecraft, the antennas are separated by 120° clock angle. Although not shown in Fig. 5, the "Z" antenna passes closest to the IMPACT instrument boom Luhmann et al. 2007.

A transformation matrix

$$\mathbf{M}_1 = \begin{pmatrix} -\frac{1}{\sqrt{3}} & -\frac{1}{\sqrt{3}} & -\frac{1}{\sqrt{3}} \\ -\frac{1}{\sqrt{2}} & \frac{1}{\sqrt{2}} & 0 \\ \frac{1}{\sqrt{6}} & \frac{1}{\sqrt{6}} & -\sqrt{\frac{2}{3}} \end{pmatrix} \tag{2}$$

takes a vector from the antenna coordinate system to the spacecraft coordinate system $\vec{x}_{\text{sc}} = \mathbf{M}_1 \cdot \vec{x}_{\text{ant}}$. This transformation does *not* include the perturbations of the antenna pattern due to electrical coupling with spacecraft structure (i.e. the "effective" antenna vectors); that effect is discussed in Sect. 5.

4.1 Stacer Antenna Elements

A stacer is a rolled, constant helical pitch, fixed diameter flat spring. The strip width, thickness, roll diameter, and helical pitch are selectable, allowing a stacer to be tailored for optimum properties for each application. Stacers range in size from 1–10 meters in length, from 4–55 mm in diameter at the tip, and can provide extensive force from almost nothing to >200 N. Trade studies can balance mass versus length, force, stiffness, etc. In the

Fig. 3 CAD drawing of an antenna unit, without covers, showing the flyweight brake, stacer antenna element, and the deployment assist device (DAD)

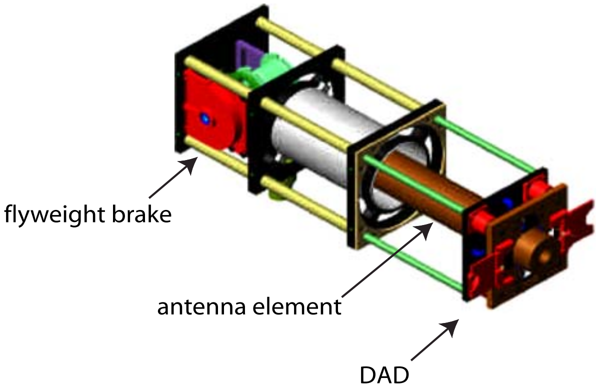

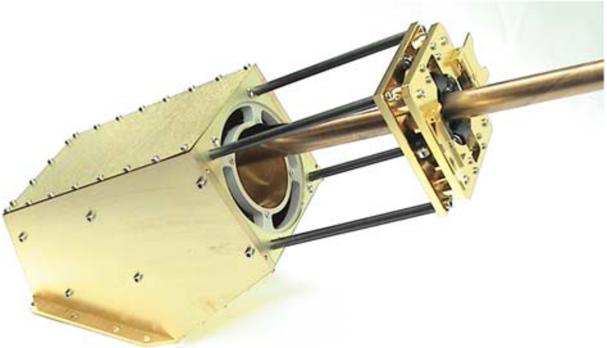

Fig. 4 A complete deployed antenna unit. The external housing is designed to point the deployed antenna

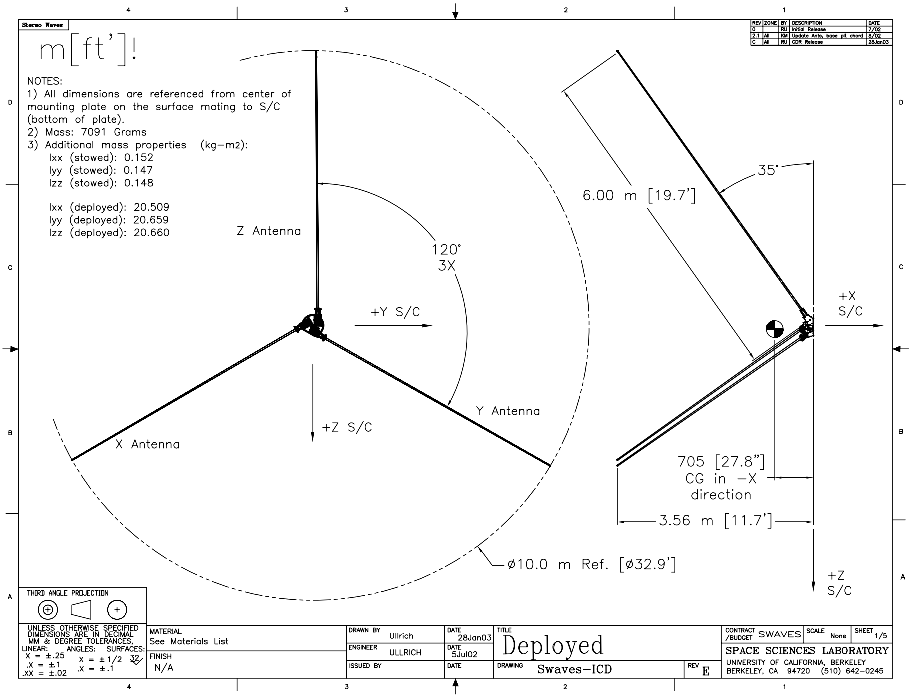

NOTES:
1) All dimensions are referenced from center of mounting plate on the surface mating to S/C (bottom of plate).
2) Mass: 7091 Grams
3) Additional mass properties (kg−m2):
Ixx (stowed): 0.152
Iyy (stowed): 0.147
Izz (stowed): 0.148

Ixx (deployed): 20.509
Iyy (deployed): 20.659
Izz (deployed): 20.660

REV	ZONE	BY	DESCRIPTION	DATE
0		RU	Initial Release	7/02
2.1	All	KM	Update Ants, base plt chord	8/02
C	All	RU	CDR Release	28Jan03

UNLESS OTHERWISE SPECIFIED DIMENSIONS ARE IN DECIMAL MM & DEGREE TOLERANCES,
LINEAR: X = ±.25 .X = ±1 .XX = ±.02
ANGLES: X = ± 1/2 .X = ±.1
SURFACES: 32
MATERIAL See Materials List
FINISH N/A
DRAWN BY Ullrich
DATE 28Jan03
ENGINEER ULLRICH
DATE 5Jul02
ISSUED BY
DATE
TITLE Deployed
DRAWING Swaves−ICD
REV E
CONTRACT /BUDGET SWAVES
SCALE None
SHEET 1/5
SPACE SCIENCES LABORATORY
UNIVERSITY OF CALIFORNIA, BERKELEY
BERKELEY, CA 94720 (510) 642−0245

Fig. 5 The deployed configuration of the S/WAVES antennas. The deployed antennas form vertices meeting at the corner of a cube. The antennas are labeled X, Y, and Z and the spacecraft coordinate system is defined with $+X_{S/C}$, $+Y_{S/C}$, and $+Z_{S/C}$

last 30 years, more than 650 units have been used in aerospace applications, from sounding rocket sensors to gravity gradient booms with large masses on the end. Most applications use the stacer as a boom with the sensor(s) mounted directly on it; for the S/WAVES antennas the stacer itself is the antenna element. For this program, the selected spring material was the traditional beryllium copper (Be–Cu). This alloy (CDA172, XHMS temper) has a modulus (E) of ∼131 GPa and a yield strength of ∼1,200 MPa. To ensure repeatability of deployment, the hidden edge of the strip is coated with PermaSlik RMAC: molybdenum

Fig. 6 Beryllium copper stacer antenna element. The aspect ratio is exaggerated here for display purposes

disulfide in an epoxy binder. To minimize the optical intrusions of the stacer antennas for the other instruments on the spacecraft, the natural matte copper-colored surface was selected.

At deployment, the formation of the stacer starts with the initial coil winding inward from the (larger diameter) storage canister onto a cylindrical tip piece, which is slightly larger than the free-coil diameter of the stacer. Thus the stacer grabs the tip piece tightly, and as the tip deploys, the subsequent coils stack up on the prior, producing the characteristic spiral appearance. The typical helix angle provides for significant overlap, such that a section taken at any point along the stacer would yield at least two thicknesses of strip material. Since the outer layer of strip is rolled to the same diameter as the inner layer, the outer grips the inner with a force normal to the surface. Thus between layers significant inter-coil friction exists and prevents inter-coil slipping for small disturbances. This gives the stacer one of its more useful properties: it behaves as a thin-walled tube for small displacements, with similar bending strength and stiffness. If a larger displacement occurs, the coils slip, dissipating the strain energy, serving as a friction damper. The damping ratio value is typically 5–15% for the non-slipping regime, and can reach 30–40% with the slipping. Of course, the displacement limit is buckling, as any tube would experience when the material is taken beyond its yielding strength.

The motive force for the deployment is the stored strain energy that is input to the system when the stacer is stowed. The strip is flexed against the inner wall of the canister, laying each coil inside its predecessor, and expanded tightly against the inside of the can.

When deployed, the S/WAVES stacer antenna elements are approximately 6 m long with a tip diameter of 15.2 mm and a base diameter of 32 mm; this gives a surface area of about 0.45 m^2. The mass of each stacer element is approximately 1 kg.

When compressed (stowed) it is a very compact package: the 6 m element fits in a cylinder 53 × 106 mm long. When released, this stored strain energy is reclaimed, giving the motive effort needed to extend the stacer along its path. The stacer generates a higher force at the beginning of stroke which drops off at the end of stroke. When stowed, the stacer is in a “meta-stable” state. If left unconstrained, it could deploy in either direction, therefore a back plate on the canister is required to ensure the correct deployment direction. To ensure that it deploys properly, with a well-formed helix gripping tightly on the tip piece, a deployment assist device (DAD) is incorporated.

4.2 Deployment Assist Device (DAD)

The Deployment Assist Device (DAD) guides the stacer element from its stowed configuration and also acts to provide effective rigidity to the deployed element by securing it at a second point.

As mentioned, a stacer when stowed in its canister is in a meta-stable configuration. It is wound out against the inner wall of the canister, and does not immediately develop a large force in the deployment direction. At initial motion, the stacer moves slowly in the axial

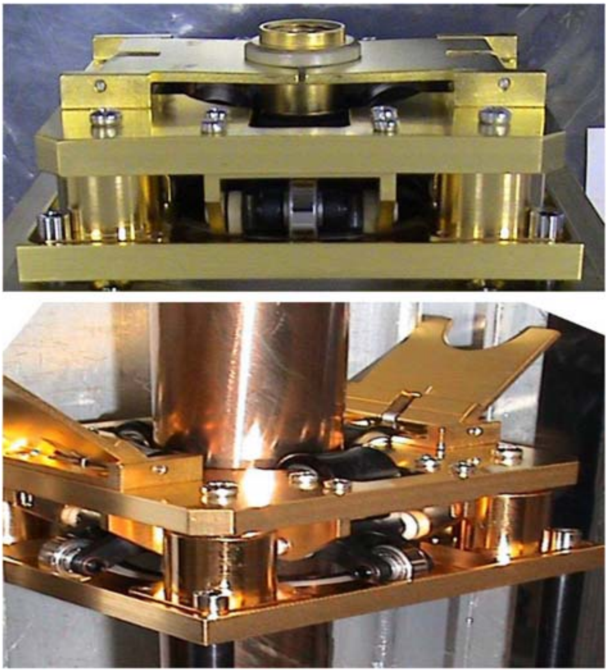

Fig. 7 Deployment assist device (DAD). The *upper panel* shows the DAD before antenna deployment, with the antenna tip piece held by trap doors. In the *lower panel*, the fully deployed antenna is held by roller nozzles, electrically isolated from the DAD itself

direction as the first coil pivots to grip the tip piece. The coils then form one at a time in the center of the can, pushing the previously formed coils outward along the deployment axis. It has been seen through many years of development that the stiffness and repeatability of the formed stacer can be enhanced by the use of an initiator that gives the first couple of coils a velocity boost. This is achieved by incorporating a spring-driven set of rods that are temporarily connected to the tip piece via trap doors. These springs pull the stacer out of the canister with ∼90 N force, giving a strong initial impulse to the deployment. By the time the DAD reaches end of its 100 mm stroke and stops, the stacer has reached full velocity and the flyweight brake is spun up to speed. The stacer, continuing to deploy, pops the doors open, allowing it to continue deploying to full length unobstructed.

At this time the second feature of the DAD becomes functional: the roller nozzle is in contact with the outer surface of the stacer, giving strong radial support with low longitudinal drag. As the diameter of the stacer increases, the roller nozzle expands to accommodate it. The roller nozzle incorporates a set of four radially symmetric roller bearings that are mounted into a bell crank mechanism. The upper and lower plates of the nozzle are joined via springs, and supply the centering force for the rollers. The stiffness of the nozzle is set by the spring value, and is tailored for each application. As the stacer deploys and its diameter increases, the rollers are forced apart, compressing the springs, centering the stacer. Any offset from center lowers the force on the side away from the offset, and increases by a similar amount the side in the offset direction, giving a double centering force. Axial drag is typically less than 2 N while the centering force is ∼50 N. The DAD is shown in Fig. 7.

4.3 Shape Memory Alloy Release (SMAR)

Deployment is initiated when the Shape Memory Alloy Release (SMAR) is triggered. The SMAR uses the interesting phase change properties of a 50% titanium–50% nickel alloy

Fig. 8 SMAR and filter board

(trade named Nitinol initially) to provide the actuation of each of the S/WAVES antenna elements. This device, pioneered by TiNi Aerospace in cooperation with UCB-SSL, takes advantage of the ∼4% dimensional change in the drawn alloy wire when heated above its transformation temperature. This lengthening allows a ball detent mechanism to release a spring-loaded retracting pin. Since there was a low design load requirement (@ 50 Gs), a standard P10-605-4.5RS with roller tip providing 45 N of retraction force was selected. When an electric current is passed though the Ti–Ni wire, it heats up, changes phase, elongates, and releases the pin, which retracts, allowing the stacer to deploy. The main benefit of using an SMAR, aside from increased safety as no explosives are incorporated, is that the flight unit can be tested over and over again (hundreds of cycles), and can be simply reset using a hand tool, with no temperature- or time-dependent constraints. A filter circuit was inserted in line with the SMAR trigger wires to remove any noise from the spacecraft firing circuits that could be conducted into the antennas. The SMAR and filter are shown in Fig. 8.

4.4 Flyweight Brake

After the SMAR has been triggered, kick springs push the DAD rods out of the tubes giving the stacer a good initial velocity. The stacer continues to recover the stored strain energy as it uncoils during extension, so the deployment velocity would continue to accelerate unless/until a balance between drag and push is achieved. This balance is never reached by the bare stacer, so the deployment velocity unchecked can reach a run-away condition, with the possible issues of rivet shearing, strip tearing and resultant separation from the assembly or other damage as consequences. As with every stacer, a means to limit deployment velocity (or travel) is incorporated. For the S/WAVES Antennas, a flyweight brake mechanism is used to govern the stacer velocity. Similar to the device found on dial telephones that regulates the rotation rate, the flyweight brake supplies braking force proportional to the rotational speed of its weight assembly. At the beginning of deployment, the FWB is not up to speed, and provides no resistive drag as the brake shoes are not touching the brake drum. Once the DAD has completed its stroke, the FWB is up to speed and the shoes are engaged. If the force (speed) increases, the flying brake shoes are centripetally accelerated against the brake drum harder, increasing the braking force and slowing the rotational velocity. As the speed

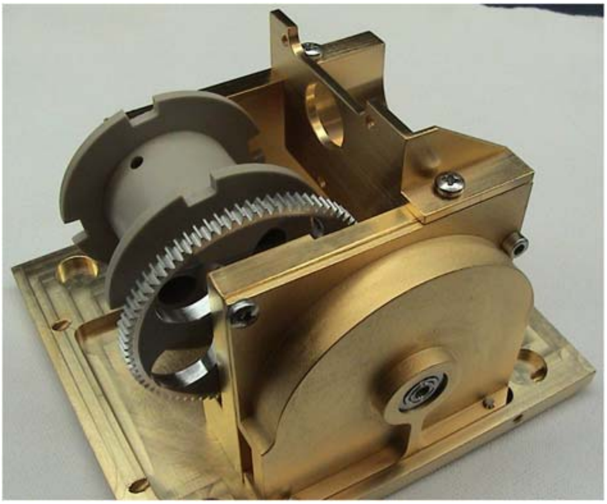

Fig. 9 Flyweight brake (without the Dacron string)

then decreases, the centripetal acceleration of the shoes decreases, allowing the deployment speed to stabilize. Over a wide range of forces, the brake typically can control the speed to $\pm 10\%$. For S/WAVES, a deployment velocity of ~ 2 m/s was chosen. This allows a strong momentum to build, but is slow enough to be controlled, preventing damage to the stacer at the end of travel. The stacer tip piece is connected to the brake assembly by a woven Dacron (parachute “shock”) cord. To dissipate the final momentum at the end of the stroke, the Dacron cord stretches, absorbing the shock from the stacer coming to a sudden halt. The flyweight brake mechanism is shown in Fig. 9.

4.5 Mechanism Operation and Safety

When the SMAR is triggered, the restraint pin pulls out of the tail of the stacer tip piece. The deployment assist device (DAD) gives the stacer an initial kick for the first 100 mm of travel. By this time, the initial coils of the stacer are fully formed around the tip piece, and the flyweight brake has been spun up to speed, limiting the speed of deployment to ~ 2 m/s, giving a total deployment time of ~ 3 s.

The stacer is *not* retractable once deployed. Re-stowing is achieved by removal from the spacecraft, and hand retraction whereby the stacer is compressed into its canister and the lanyard and flyweight brake are rewound. Finally, the SMAR is reset, reinstalled, and the spool lock is set.

The primary method for retaining the stacer is the SMAR. It has a stainless steel pin that is inserted into the tail of the stacer tip piece. It retracts only upon spacecraft command, and is the method for deployment on orbit. A safety pin inserts into the rear part of the tip piece to provide a redundant method of keeping the stacer from deploying at undesired times. This pin is a red-tag item, meaning it must be removed prior to launch. It can be removed from the exterior of the unit. Additionally, an RF tight test cap incorporating a method of attaching to the antenna to provide input for instrument verification and calibration, has the ability to capture a released stacer, should there be an unexpected deployment event when the safety pin is removed. The test cap is also a red-tag item. This three-tier approach gives the antennas excellent defense from unexpected deployment and potential contact with support personnel.

4.6 Verification

The S/WAVES qualification activities were based on GEVS SE, as modified by JHU-APL for mission-specific needs. The test regime selected for the STEREO mission was Protoflight, meaning new (unflown or non-heritage) hardware is tested with a combination of prototype (EM) levels (i.e. temperature or vibration) with flight (FM) durations. This method is typically used to shorten development times by eliminating the engineering/qualification model fabrication and test period. However, the S/WAVES Team did build up an engineering model, and tested it to the protoflight levels. The main changes and additions to the testing regimen: Level 300 cleanliness, UV + Visible light inspection, no silicones used for fabrication, and testing for silicone residuals. Vibration levels were taken from the Delta II users manual modified by APL analysis for the stacked configuration.

Validation of deployables must balance the desire to prove beyond question that the mechanism will deploy in space with the requirement to avoid wear and damage to the device. This breaks down to: How many times? GEVS provides a minimum number, and each program defines how many additional operations are required. There is a concern regarding wear margin, too. The design must show that it is sufficiently robust to survive testing and flight without degradation. The EM served this purpose, getting many deployments more than the FMs did. After inspection of the EM, a test plan was developed, reviewed, and implemented. The EM was deployed more than 15 times throughout the program while the FM units were deployed 4 times: 2 in ambient conditions and 2 in thermal vacuum.

Testing large deployables in a simulated space environment is difficult, and ensuring that the test actually verifies functionality is critical. Deploying the antennas horizontally was chosen as it is easy to develop a 6 m long test rig that rests on stands, and can be used in thermal vacuum deployment tests. This consisted of an aluminum track, with a low-friction trolley to guide the tip piece down its length. A 6 m long × 210 mm diameter tube was attached to an existing thermal vacuum chamber allowing the deployment track to be installed inside for thermal vacuum deployments. The length measurements and deployment times are more accurate horizontally than if deployed vertically as the stacer behaves more uniformly when not subjected to an axial gravity load. Each antenna assembly was subjected to seven hot/cold cycles at high vacuum (10^{-6} Torr). At the final temperature cycle, each unit was deployed once hot and once cold.

The first natural (cantilever) frequency of each antenna element was measured using a small accelerometer, after the second ambient deployment. Measurements of the cantilever frequency f_0 and damping ratio showed a family of values clustering around $f_0 \approx 0.6$ Hz and an average damping ratio of 5.2%.

5 Base Capacitance Measurements

As discussed in Sect. 2, the gain of the antenna system at high frequencies is determined by the level of stray capacitance. In this context, sources of stray capacitance are the "base" capacitance, capacitance in the semi-rigid coax cables between the antennas and preamps, and the input capacitance of the preamps. Cable and preamp-input capacitance are measured easily in the lab: for S/WAVES, cable capacitance is approximately $C_C \approx 13$ pF and the measured input capacitance of the preamps is $C_{\mathrm{PA}} \approx 22$ pF.

The base capacitance is more difficult to measure, since an accurate measurement requires that the antenna be deployed and it is measured in parallel with the antenna free-space capacitance C_A (1).

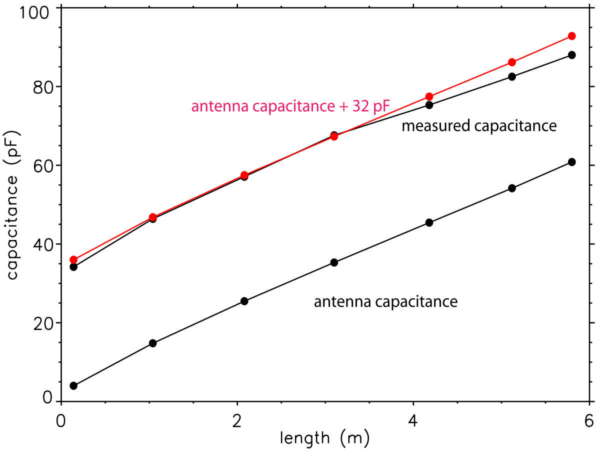

Fig. 10 Measurements of the capacitance of an S/WAVES antenna. The *upper black points* are measured capacitances vs antenna length. The *lower black points* are the theoretical expectation C_A for a monopole against a ground plane (1). The *red points* are C_A plus 32 pF, which represents the base capacitance

To understand the base capacitance, an S/WAVES flight spare unit was deployed in the high bay at the Space Sciences Laboratory at UC Berkeley. The unit was mounted to deploy normal to a 1 m × 1 m horizontal conducting plane and suspended from the tip by a 2 m nonconducting string from a crane. The exterior of the antenna unit was to connected to the ground plane. The capacitance was measured at the SMA connector on the antenna box using a BK Precision 878 LCR meter (operating at 1 kHz). Following this measurement, the antenna was lowered, 1 m of stacer was cut from the end, the length and diameter were measured, and it was suspended and tested again. This process was repeated until only 14 cm of the stacer antenna extended beyond the base of the deployment unit.

The results of these measurements are shown in Fig. 10. The upper set of black dots shows the measured capacitance as a function of antenna length. The lower black dots show the theoretical free-space antenna capacitance C_A (1) as a function of length (and radius, which varied at the antenna length was cut). The set of red dots shows the free-space capacitance C_A *plus* 32 pF, which agrees well with the measured values. For antenna lengths greater than 4 m, the theoretical curve overestimates the measured capacitance. This is because (1) is valid for an infinite groundplane and this approximation becomes weaker with longer antenna lengths.

These measurements suggest a value of $C_B \approx 32$ pF for the base capacitance. Then the total stray capacitance of an antenna unit is $C_{\text{stray}} \approx C_B + C_C + C_{PA} \approx 32\text{ pF} + 13\text{ pF} + 22\text{ pF} = 67\text{ pF}$, which gives an antenna gain of approximately $G \approx C_A/(C_A + C_{\text{stray}}) \approx 1/2$.

6 Modeling of the S/WAVES Antennas

The three monopole antenna elements are used by S/WAVES to sense the electric field of radio waves. Due to radiation coupling between each other and with the spacecraft body and appendages the reception properties of the antennas differ from what one would expect from the respective "stand-alone" monopoles. In the present context the so-called effective length vector $\vec{h}$ is most suitable to represent the reception properties. It comprises the electrically effective length and direction of an antenna, thereby representing the relation $V = \vec{h} \cdot \vec{E}$ between the voltage V received from an electromagnetic wave and its electric field $\vec{E}$. For the mentioned reasons the effective length vectors $\vec{h}_X$, $\vec{h}_Y$ and $\vec{h}_Z$ of the S/WAVES antennas

X, Y, and Z deviate considerably from the respective mechanical elements. Several methods are applied to determine these vectors as well as the antenna capacitances. The focus is on the quasi-static frequency range, where the wavelength is much greater than the dimension of the antenna-spacecraft system. In this range, the effective length vectors are real and constant quantities, therefore in-flight calibration is feasible (whereas at higher frequencies, the antenna pattern is complicated and modified by spacecraft structure—this makes in-flight calibration very difficult).

6.1 Simulations and Rheometry Measurements

Computer simulations and rheometry measurements are performed, providing completely independent approaches. The computer simulations are based on wire-grid modeling, where the whole spacecraft structure is represented by a mesh of wires covering the spacecraft surface. Several smaller features which show no significant influence on the results were omitted in the final modeling. The main features which affect the reception properties most are the solar panels, the high-gain antenna and the IMPACT boom (Fig. 11). For the rheometry measurements, a more detailed model is devised (Fig. 12). Rheometry is an electrolytic tank measurement adapted to antenna analysis, which was developed at the Observatoire de Paris-Meudon in the early 1970s. It proved very suitable for the determination of effective length vectors of many spaceborne antenna systems. For the measurement of the S/WAVES antennas a similar set-up was used as for the Cassini/RPWS antennas (Rucker et al. 1996) at Graz and a new rheometry facility was built at UC Berkeley. Both rheometry models were 1/30 scale.

The results of the numerical and the experimental approach agree within the inherent inaccuracy of the methods. The table in Fig. 14 shows the averages of the effective length vectors as obtained by the two methods, from both Graz and Berkeley. The Berkeley results include only rheometry results, as no wire grid simulations were done at Berkeley. The accuracy is about 5–6 degrees for directions and 5% for the effective lengths. The mechanical antenna elements are also shown for comparison. The spacecraft coordinate axes are defined as follows: The X-axis is directed opposite to the boom, the Y-axis parallel to the axes of the solar panels and directed as shown in Fig. 10, the Z-axis completes the right-handed triad. The antenna axes are given in spherical coordinates with regard to the reference frame ($-Z$,

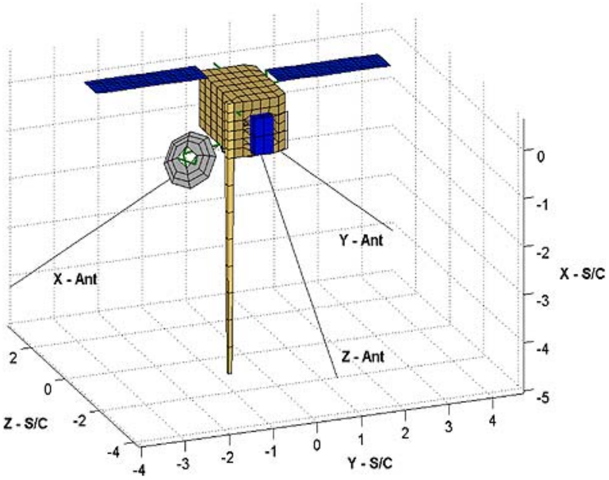

Fig. 11 Wire-grid model of STEREO spacecraft with S/WAVES antennas (*red*). The components which affect the antenna reception properties most are the solar panels (*blue*), the high gain antenna (*gray*), and the IMPACT boom (*tapered vertical rod*)

Fig. 12 STEREO spacecraft model used for the rheometry measurements in Graz. Only two of the S/WAVES antennas are visible

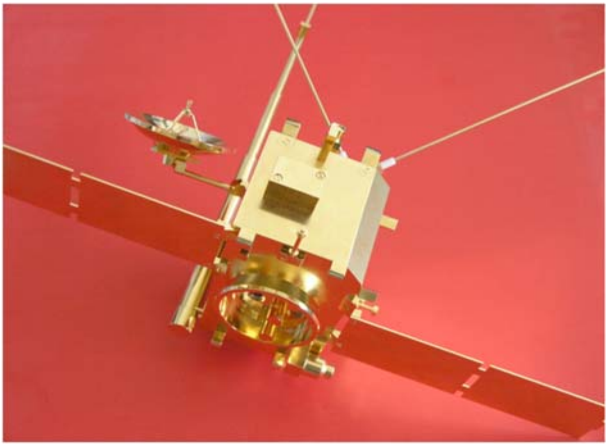

Fig. 13 Definition of spherical coordinates θ and ϕ in the spacecraft-fixed reference frame for the representation of effective and mechanical antenna axes (in the latter case the origin is identified with the respective antenna feed)

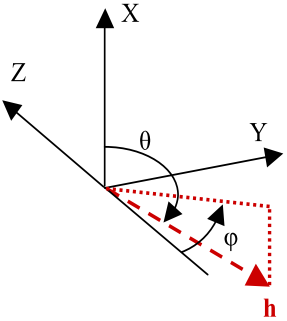

Y, X), i.e. colatitude θ from $+X$ and azimuth ϕ from $-Z$ towards Y (Fig. 13). The Graz results are also given for open and loaded antenna ports. In this context the loads are the base capacitances C_B of the respective antennas, consisting of receiver input capacitances, cable, and mounting capacitances. Measurements of the individual capacitances gave the same total $C_B = 90$ pF for each antenna, which was implemented in both methods. The results show clearly that the effective lengths for open ports are about half of the respective mechanical antenna lengths, which is a well-known result for the ideal dipole. However, the effective axes significantly differ from the respective mechanical ones. One also can clearly see that the base capacitances further reduce the effective lengths dramatically, and even cause an offset of the effective antenna directions. This effect is due to the radiation coupling between the antennas (directly or via the spacecraft body) and confirms the importance of the base capacitances. A detailed study of the antenna system including the dependence of the reception properties on various spacecraft features (e.g. the rotation angle of the high gain antenna which gradually changes in the course of the mission) will be published in a separate paper.

To transform from measured voltages V_X, V_Y, V_Z on the antennas (where X, Y, Z subscripts denote the antenna coordinate system) into an "electric field" in the spacecraft coordinate system, a transformation

		h [m]	θ [deg]	ϕ [deg]
Physical antennas	X	6.00	125.3	−120.0
	Y	6.00	125.3	120.0
	Z	6.00	125.3	0.0
Open feeds (Graz)	$\mathbf{h}_{\mathrm{X},0}$	2.98	126.0	−141.2
	$\mathbf{h}_{\mathrm{Y},0}$	3.85	118.8	128.7
	$\mathbf{h}_{\mathrm{Z},0}$	2.34	133.0	21.5
Open feeds (UC Berkeley)	$\mathbf{h}_{\mathrm{X},0}$	3.04	127.0	−148.0
	$\mathbf{h}_{\mathrm{Y},0}$	3.95	120.8	123.6
	$\mathbf{h}_{\mathrm{Z},0}$	2.45	132.6	22.6
w/base caps (Graz)	$\mathbf{h}_{\mathrm{X}}$	1.17	120.2	−135.0
	$\mathbf{h}_{\mathrm{Y}}$	1.44	114.5	127.1
	$\mathbf{h}_{\mathrm{Z}}$	0.97	124.5	15.5

Fig. 14 Mechanical antenna lengths and directions of S/WAVES antennas X, Y, and Z compared with the effective length vectors for open feeds and for a load (base capacitance) of 90 pF at each antenna. The given results are averages of rheometry measurements and wire-grid simulations, with the exception of the Berkeley results, which include only rheometry measurements

$$\begin{pmatrix} E_x \\ E_y \\ E_z \end{pmatrix}_{\mathrm{SC}} = \mathbf{M}_2 \cdot \begin{pmatrix} V_X \\ V_Y \\ V_Z \end{pmatrix}_{\mathrm{ANT}},$$

where

$$\mathbf{M}_\mathbf{2}^{-\mathbf{1}} = \begin{pmatrix} h_X \cos\theta_X & h_X \sin\theta_X \sin\varphi_X & -h_X \sin\theta_X \cos\varphi_X \\ h_Y \cos\theta_Y & h_Y \sin\theta_Y \sin\varphi_Y & -h_Y \sin\theta_Y \cos\varphi_Y \\ h_Z \cos\theta_Z & h_Z \sin\theta_Z \sin\varphi_Z & -h_Z \sin\theta_Z \cos\varphi_Z \end{pmatrix}$$

can be applied using the effective lengths and angles from the table in Fig. 14.

6.2 Anechoic Chamber Measurements at High Frequencies

S/WAVES measurements also include the Fixed Frequency Receiver (FFR) which operates at high frequencies above the antenna resonance. For the FFR, two monopoles are used as a dipole and any combination is selectable (i.e. dipole X–Y, Y–Z, or X–Z); these dipoles will have an electrical resonance around 25 MHz while the FFR operates at 30.025 or 32.025 MHz. Furthermore, at these frequencies it is no longer possible to neglect the influence of the spacecraft and its appendages. These effects may give rise to unexpected secondary lobes and cause lower gains in the primary lobes.

To understand these effects, an electrical model of the STEREO spacecraft was built at 1/10th scale and antenna patterns were measured in an anechoic chamber at the CNES facility in Toulouse, France. In order to keep the same ratio of the wavelength to spacecraft dimension, the testing frequencies are multiplied by 10. The testing campaign consisted of measurements on the three dipoles at various frequencies (300, 320, 340 and 360 MHz) and various orientations of the scale model. Facilities consist of an anechoic chamber including

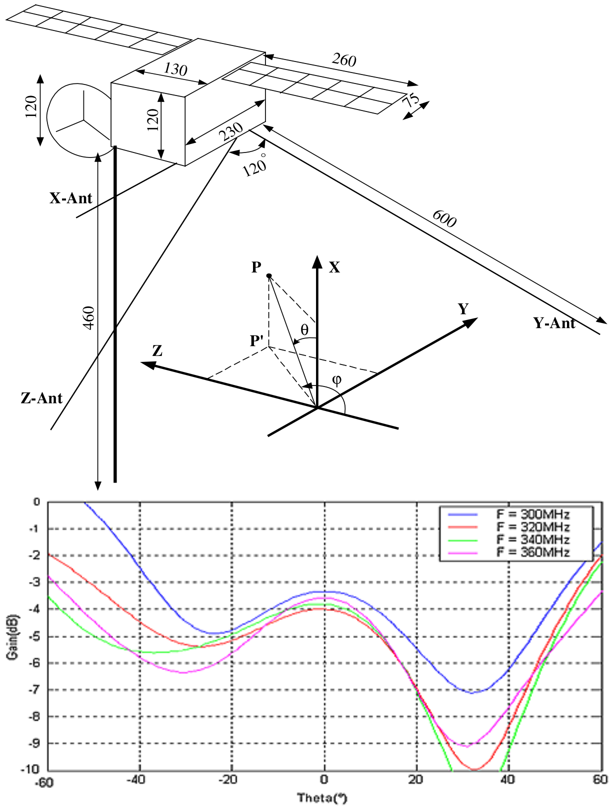

Fig. 15 Antenna gain at high frequencies from anechoic chamber measurements with a scale model. The coordinate system is shown in the spacecraft schematic (*upper panel*)

a large parabolic reflector providing a plane wave. Both components of the electric field were measured in the horizontal and vertical position (E_h and E_v), which are associated using (2):

$$E_{dB} = 10\log\left(E_h^2 + E_v^2\right) \tag{3}$$

with E_h and E_v in V/m. Finally, the absolute gain was determined and calibrated by comparison to a reference antenna. As an example, the Fig. 15 shows the resulting radiation patterns of the dipole 1–2. This is plotted in a Cartesian representation, where the X-axis is the θ angle from $-60°$ to $+60°$ and the Y-axis is the antennas gain for a given orientation. More specifically we are interested in the antenna gain in direction of the sun (i.e. for θ neighboring 0°). Taking into account the localization of the antennas on the (backside of the) spacecraft, it is clear that their gain is not optimal in direction of the Sun. For $\theta = 0°$, the gain disparities are about 2 dB depending on the frequency. The gain is between -2 dB and -4 dB for dipoles 1–2 and 1–3, and slightly weaker for the dipole 2–3 which is in the shadow of the solar panels. Since the gain at the frequencies 300 MHz and 320 MHz are less disturbed by the spacecraft configuration (especially true for dipole 2–3), the corresponding frequencies (30.025 and 32.025 MHz) were chosen for the design of the FFR.

7 In-Flight Antenna Calibration

In order to calibrate the STEREO/WAVES electrical antenna system, in-flight antenna calibration is necessary. In-flight calibration includes the characterization of the equivalent effective dipole antenna directions and the calibration of the antenna system gain (antenna capacitance, base capacitance and antenna effective lengths). The antenna gain and the antenna and base capacitances are inferred using the galactic background radiation, as was done for the Cassini/RPWS electrical antenna system (Zarka et al. 2004). The effective antenna directions are calibrated with spacecraft rolls. The methodology of this calibration is described in Vogl et al. (2004). The reference radio source used for calibration is the Earth auroral kilometric radiation (AKR). The spacecraft rolls have been programmed at about 120 R_E (Earth radii) from the Earth, so that the spacecraft is far enough from the Earth to be able to assume that the AKR sources are in the Earth direction, and that the signal to noise ratio (SNR) is high enough to get an accurate result. We assume that the position of the source is known and that the emissions are purely circularly polarized (Kaiser et al. 1978). It is then possible to invert the direction finding measurements and obtain the antenna directions and relative lengths. As described by Vogl et al. (2004), the "effective" antenna vector should ideally point towards the selected radio source twice per roll in order to perform the calibration. This ideal geometrical configuration could not be met in the case of the STEREO/WAVES antenna calibration sequences because of spacecraft pointing requirements. However, as shown by Cecconi and Zarka (2005), the data has to be carefully selected in order to get accurate calibration results. The two critical criteria are the SNR and the angular distance between the antennas and the reference radio source direction. We define α_i the angular distance between the ith antenna and the direction of the radio source, and β_{ij}, the angular elevation of the source over the plane defined by the ith and jth antennas. It has been shown by Cecconi and Zarka (2005) that the data selection for accurate antenna parameters calibration are: (a) $15^\circ < \alpha_i < 45^\circ$, $\beta_{ij} > 10^\circ$ and SNR $\geq 20\,\text{dB}$ in the case of the ith antenna direction calibration (using measurements on antenna i and j), (b) $\alpha_i > 20^\circ$, $\alpha_j > 20^\circ$ and SNR $\geq 20\,\text{dB}$, when calibrating the h_i/h_j antenna length ratio. These data selections are compatible with the spacecrafts rolls programmed for the in-flight antenna calibration of the STEREO/WAVES electrical antenna system.

8 Summary and Early Results

The S/WAVES antennas completed qualification and acceptance verification for use in flight for the NASA STEREO mission and were integrated onto the spacecraft in early 2005. STEREO launched on October 25, 2006, and the S/WAVES instrument was powered up on October 27. The S/WAVES antennas were deployed successfully on the Ahead spacecraft on October 27, 2006, at approximately 16:42, 17:00, and 17:24 UT (X, Y, and Z respectively). Shortly after deployment, spacecraft controllers noted a slight ($\sim 10^{-5}$ radians amplitude) spacecraft wobble at the antenna cantilever frequency (approximately 0.6 Hz); the spacecraft attitude control system has been adjusted to correct for this motion. On October 29, 2006, the Behind spacecraft antennas were deployed successfully (at 21:24, 21:59, and 22:22 UT for X, Y, and Z). Early data confirm that the S/WAVES antennas work well.

Acknowledgements S/WAVES antenna design and fabrication was funded at UC Berkeley under NASA contract NAS5-03076. Several people at UC Berkeley helped to develop the S/WAVES antennas, chief among them are Paul Turin, Ken McKee, David Pankow, and Kate Harps. We thank Paul Buchanan, Therese Erigo, and Steve Wasserzug from NASA/GSFC.

Part of the S/WAVES antenna modeling program was financed by the Austrian Research Promotion Agency (FFG) in the framework of the Austrian Space Applications Program (ASAP) under contract FFG 811682. The Graz rheometry model was manufactured by H. Reiterer, Prototypenbau Meister. We thank H.O. Rucker and G. Fischer for valuable support and discussions on the antenna analyses

References

C.A. Balanis, *Antenna Theory* (Wiley, New York, 1997)
S.D. Bale, D. Burgess, P.J. Kellogg, K. Goetz, S.J. Monson, J. Geophys. Res. **102**, 11–281 (1997)
S.D. Bale, P.J. Kellogg, K. Goetz, S.J. Monson, Geophys. Res. Lett. **25**, 9 (1998)
S.D. Bale, M.J. Reiner, J.-L. Bougeret, M.L. Kaiser, S. Krucker, D.E. Larson, R.P. Lin, Geophys. Res. Lett. **26**, 1573 (1999)
S.D. Bale, P.J. Kellogg, F.S. Mozer, T.S. Horbury, H. Reme, Phys. Rev. Lett. **94**, 215002 (2005)
J.-L. Bougeret et al., Space Sci. Rev. (2007, this issue)
I.H. Cairns, D.B. Melrose, J. Geophys. Res. **90**, 6637 (1985)
B. Cecconi, P. Zarka, Radio Sci. **40**, RS3003 (2005). doi:10.1029/2004RS003070
J. Fainberg, L.G. Evans, R.G. Stone, Science **178**, 743 (1972)
R.J. Fitzenreiter, A.J. Klimas, J.D. Scudder, Geophys. Res. Lett. **5**, 496 (1984)
M.V. Goldman, Rev. Mod. Phys. **56**, 709 (1984)
R.J.L. Grard, J. Geophys. Res. **78**, 2885 (1973)
D.A. Gurnett, *Principles of Space Plasma Wave Instrument Design*. AGU Geophysical Monograph, vol. 103 (1998), p. 121
P. Harvey, F.S. Mozer, D. Pankow, J. Wygant, N.C. Maynard, H. Singer, W. Sullivan, P.B. Anderson, R. Pfaff, T. Aggson, A. Pedersen, C.-G. Falthammar, P. Tanskannen, Space Sci. Rev. **71**, 583 (1995)
M.L. Kaiser, J.K. Alexander, A.C. Riddle, J.B. Pearce, J.W. Warwick, Geophys. Res. Lett. **5**, 857 (1978)
P.J. Kellogg, Astron. Astrophys. **169**, 329 (1986)
P.J. Kellogg, S.D. Bale, J. Geophys. Res. **106**(18), 721 (2001)
P.J. Kellogg, S.D. Bale, F.S. Mozer, T.S. Horbury, H. Reme, Astrophys. J. **645**, 704 (2006)
D. Krauss-Varban, D. Burgess, J. Geophys. Res. **96**, 143 (1991)
D.E. Larson, R.P. Lin, J. Steinberg, Geophys. Res. Lett. **27**, 157 (2000)
M.M. Leroy, A. Mangeney, Ann. Geophys. **2**, 449 (1984)
J.G. Luhmann et al., Space Sci. Rev. (2007, this issue). doi:10.1007/s11214-007-9170-x
N. Meyer-Vernet, C. Perche, J. Geophys. Res. **94**, 2405 (1989)
J.C. Novaco, L.W. Brown, Astrophys. J. **221**, 114 (1978)
A. Pedersen, F. Mozer, G. Gustafsson, *Electric Field Measurements in a Tenuous Plasma with Spherical Double Probes*. AGU Geophysical Monograph, vol. 103 (1998)
H.O. Rucker, W. Macher, R. Manning, H.P. Ladreiter, Radio Sci. **31**, 1299 (1996)
D. Vogl, B. Cecconi, W. Macher, P. Zarka, H.P. Ladreiter, P. Fedou, A. Lecacheux, T. Averkamp, G. Fischer, H.O. Rucker, D.A. Gurnett, W.S. Kurth, G.B. Hospodarsky, J. Geophys. Res. **109**, A09S17 (2004). doi:10.1029/2003JA010261
C.S. Wu, J. Geophys. Res. **89**, 8857 (1984)
P. Zarka, B. Cecconi, W.S. Kurth, J. Geophys. Res. **109**, A09S15 (2004). doi:10.1029/2003JA010260